ADVANCED ENERGY MATERIALS
www.advenergymat.de

A Hybrid Biofuel Cell with High Power and Operational Stability Using Electron Transfer-Intensified Mediators and Multi-Interaction Assembly

Younjun Jang, Tae-Won Seo, Junha Pak, Moon Kyu Park, Jeongyeon Ahn, Gee Chan Jin, Seung Woo Lee, Yoon Jang Chung, Young-Bong Choi,* Cheong Hoon Kwon,* and Jinhan Cho**

Biofuel cells (BFCs) offer an eco-friendly route to convert biochemical energy into electricity. However, their performance is hindered by insufficient enzyme immobilization as well as limited electron transfer within the enzymatic electrode. While the incorporation of redox mediators (RMs) into enzyme layers has been shown to improve BFC performance through enhanced electron transfer, progress has plateaued in the last decade. Herein, a major breakthrough is presented realized by a novel strategy that exploits electron transfer-intensified RM layers. Metal nanoparticles covalently bridged between neighboring RMs facilitate electron transfer ubiquitously. Electron transfer characteristics are enhanced not only within the RM layers themselves, but also at the glucose oxidase (GOx)/host electrode and GOx/GOx interfaces. This leads to a remarkable performance boost in the enzymatic anode. A hybrid BFC constructed with innovative anode and Pt-based cathode exhibits a striking combination of high power output (2.3 and 8.5 mW cm^{-2} at 10 and 300 mmol L^{-1} glucose, respectively) and exceptional operational stability (≈80% and 47% power retention after 10 days and 1 month, respectively), outperforming all previously reported BFCs by a significant margin.

1. Introduction

Biofuel cells (BFCs) are capable of generating micropower using soft and compact structures, making them ideal candidates to power portable electronics and implantable medical devices that operate under mild conditions (neutral pH and ambient temperature).[1–7] Although their power output falls short of other energy storage devices such as lithium-ion batteries, supercapacitors, and traditional fuel cells, BFCs have a distinct advantage over their peers because they leverage the utilization of renewable and safe biofuels.[8–11] As such, dramatically enhancing the power output of BFCs while preserving their intrinsic merits remains a key challenge. This challenge mainly stems from the active center (flavin adenine dinucleotide, FAD) of the enzyme being buried ≈ 7–15 Å below the protein surface, which severely

Y. Jang, J. Cho
KU-KIST Graduate School of Converging Science & Technology
Korea University
145 Anam-ro, Seongbuk-gu, Seoul 02841, Republic of Korea
E-mail: jinhan71@korea.ac.kr

T.-W. Seo
Department of Chemistry
College of Science & Technology
Dankook University
119 Dandae-ro, Dongnam-gu, Cheonan-si, Chungcheongnam-do 31116, Republic of Korea

J. Pak, M. K. Park, J. Ahn, Y. J. Chung, J. Cho
Department of Chemical and Biological Engineering
Korea University
145 Anam-ro, Seongbuk-gu, Seoul 02841, Republic of Korea
E-mail: yoonjang@korea.ac.kr

G. C. Jin, C. H. Kwon
Department of Energy Resources and Chemical Engineering
Kangwon National University
346 Jungang-ro, Samcheok 25913, Republic of Korea
E-mail: chkwon2@kangwon.ac.kr

S. W. Lee
The George W. Woodruff School of Mechanical Engineering
Georgia Institute of Technology
Atlanta, GA 30332, USA

Y.-B. Choi
Department of Cosmedical & Materials
Dankook University
119 Dandae-ro, Dongnam-gu, Cheonan-si, Chungcheongnam-do 31116, Republic of Korea
E-mail: chem0404@dankook.ac.kr

The ORCID identification number(s) for the author(s) of this article can be found under https://doi.org/10.1002/aenm.202401255

DOI: 10.1002/aenm.202401255

restricts electron transfer between the enzyme and the electrode as well as between neighboring enzymes.[12] This limitation has been a major hurdle in overcoming the low power output of BFCs.

Several research efforts have focused on enhancing electron transfer between the active sites of enzymes and the host electrode to overcome such limitations in BFC performance. A popular approach involves the development of enzymatic electrodes that utilize direct electron transfer (DET), where the active centers of enzymes are positioned within electron tunneling distance of the host electrode. Although considerable progress has been made by incorporating various conductive materials (carbon nanotubes, conducting polymers, metal nanowires, metal nanoparticles (NPs), etc.) into the enzymatic layer, the power outputs of most DET-based BFCs still remain insufficient for powering even small electronic devices.[13–16]

As an alternative strategy, numerous studies have explored electrode preparation schemes that make use of mediated electron transfer (MET).[5,6,17–22] In this technique, redox-active mediator species (RMs) are implemented to shuttle electrons between the FAD centers of glucose oxidase (GOx) and the host electrode.[19–22] In particular, reports indicate that crosslinking osmium (Os)-based RMs with long spacer arms and electron-donating group (EDG) ligands (—OCH_3 or —NH_2) to enzymes via simple mechanical mixing significantly enhances electron communication with the FAD center.[23] In essence, these long RM spacer arms increase the probability for external electrons to reach the FAD center deeply buried within the enzyme. Additionally, it was shown that BFC operation voltages could be tuned by coordinating Os-based RMs with EDG ligands or electron-withdrawing group (EWG) ligands (—COOH or —Cl) for negative or positive voltage shifts, respectively.[24] Furthermore, the hydrophilic nature of the water-soluble polymer backbone in poly-Os RMs facilitates their immobilization on the enzyme and electrode surfaces.[25] Despite these strengths, the presence of unbound enzymes, the poor electrical conductivity of enzyme-RM nanocomposites, and the use of insulating crosslinkers collectively result in limited electron transfer within enzymatic electrode, which puts constraints on the final power performance of BFCs.[26–31] Although researchers have focused on developing other types of RMs that provide easier electron hopping paths to the enzymes, progress in MET-BFCs has stagnated over the past decade after the hallmark reports of a maximum power output of ≈1.5 mW cm^{-2} and operational stability of 1.1 mW cm^{-2} after 2 days.[6,29]

In this work, we introduce a novel MET-based enzymatic electrode that has exceptional electron transfer efficiency. Additionally, we demonstrate that our MET-hybrid BFC exhibits extremely high power output (≈8.5 mW cm^{-2}) and remarkable operational stability (2.6 mW cm^{-2} after 30 days). This breakthrough is achieved through the combined effects of implementing electron transfer-intensified RMs and achieving seamless interfaces between the enzyme and RM layers (**Figure 1**). We highlight the critical role of densely integrating metal NPs into the RM layers, which significantly boosts enzyme-RM interelectron transfer. Such congruent and robust nanoblending of all components within the MET electrode was accomplished through a multi-interaction-based interfacial assembly technique that utilizes complementary covalent and electrostatic interactions. The benefit of this approach is that it eliminates the need for electrochemically inactive/insulating ingredients such as polymeric cross-linking agents, distinguishing our electrode design from other conventional MET-based enzymatic anodes. As a result, the development of a hybrid BFC with exceptionally high and stable power performance is enabled. A complete hybrid BFC implementing the electrodes presented in this work exhibits a record-high power density of 8.5 mW cm^{-2} and displays excellent operational stability, maintaining ≈80% of its initial power density after 10 days of continuous operation. These values far exceed those of most conventional crosslinked MET-BFCs, which typically have much lower initial power density (0.6 mW cm^{-2}) and operational stability (drops to ≈65% of initial power density after 10 days). While BFCs are used as an example here, our approach can be generalized and extended to design and construct various electrochemical electrodes that require high electron transfer rates and favorable interfacial interactions in electrochemically active environments.

2. Results and Discussion

2.1. Fabrication of RM/Enzyme Multilayer Films

To construct the anode for the MET-hybrid BFC, we first prepared Os-based RMs (shortly Os-RMs) with cationic Os compounds (i.e., poly(N-vinylimidazole)-[Os(4,4′-dimethoxy-2,2′-bipyridine)$_2$Cl]$^{+/2+}$) synthesized by a quaternization reaction at the 4th nitrogen atom site of the imidazole groups of poly(N-vinylimidazole). In this case, the Os-RM can act as a positively charged polyelectrolyte, which has a ξ-potential value of about +4 mV in a pH 7.4 aqueous solution, as confirmed through microelectrophoresis (Experimental section, **Figure 2a**; Figure S1, Supporting Information).

Using this building block, we evaluated the adsorption behavior of consecutive electrostatic layer-by-layer (LbL) assemblies formed by positively charged RMs and negatively charged GOx layers (Figure 2b). Our investigation employed UV–Vis spectroscopy, quartz crystal microbalance (QCM), Fourier transform infrared spectroscopy in attenuated total reflection mode (ATR-FTIR), and cross-sectional field-emission scanning electron microscopy (FE-SEM) measurements. As revealed in the UV–Vis spectra of electrostatic LbL-assembled (Os-RM/GOx)$_n$ multilayers on quartz glass (Figure 2c), the intensity of the overlapped absorption peak (at 268 nm) arising from the oxidized flavin cofactor of GOx (at 277 nm) and the imidazole groups of Os-RM (at 263 nm) showed a linear increase according to the bilayer number (n) (the inset of Figure 2c; Figure S2, Supporting Information). This implies that the amount of material adsorbed per bilayer was highly regular during the LbL assembly process. The QCM data from Figure 2d illustrates the frequency ($-\Delta F$) and mass (Δm) changes as a function of layer number in the adsorbed Os-RM and GOx. Here, the mass changes were

J. Cho
Soft Hybrid Materials Research Center
Advanced Materials Research Division
Korea Institute of Science and Technology (KIST)
5 Hwarang-ro 14-gil, Seongbuk-gu, Seoul 02792, Republic of Korea

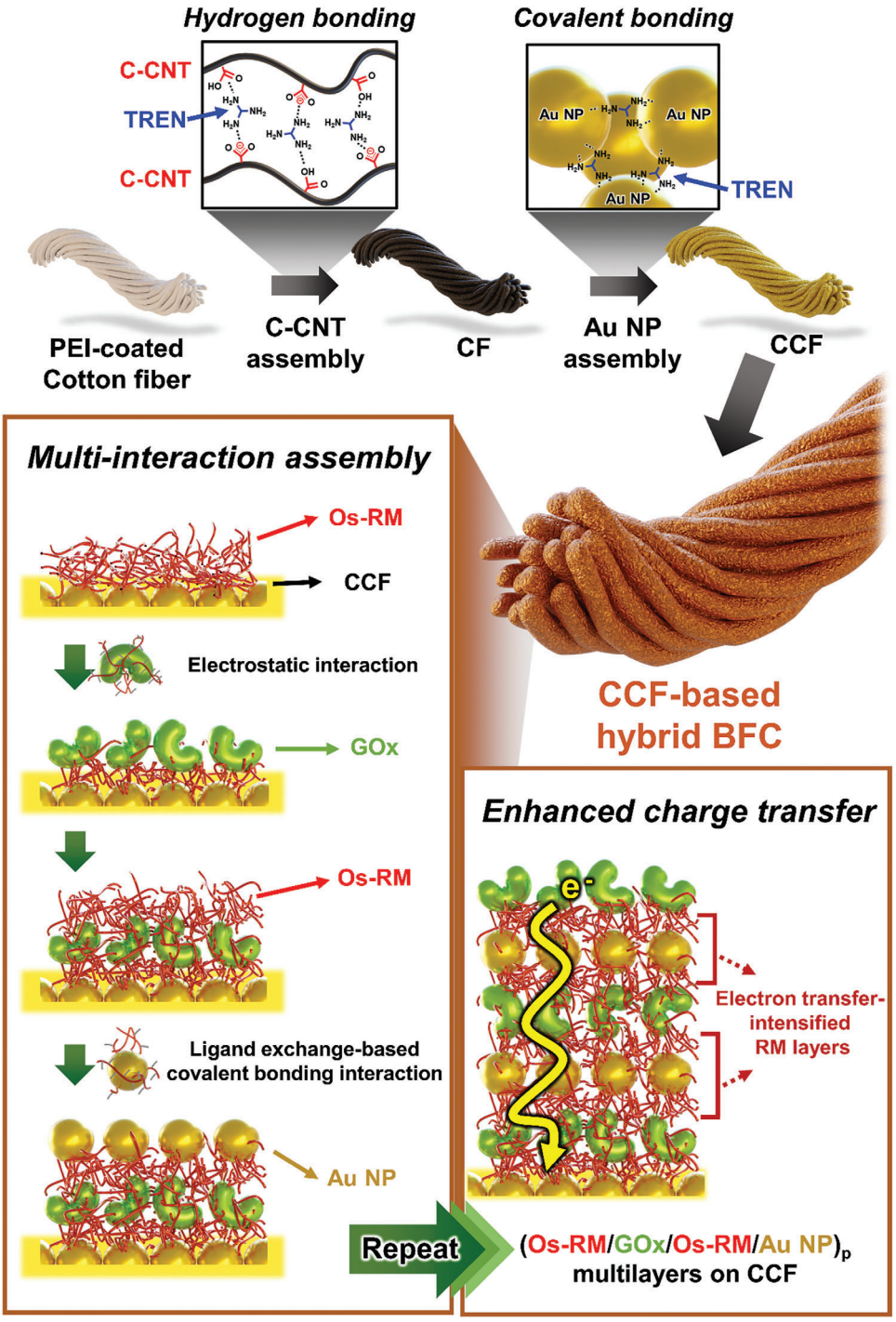

Figure 1. Schematic illustration of the preparation of high-performance hybrid BFC electrodes using the electron transfer-intensified assembly approach.

determined by measuring frequency shifts in the Os-RM and GOx layers that were adsorbed onto the QCM electrode surface using the Sauerbrey equation (refer to the Supporting Information).[32–35] The deposition of alternating Os-RM and GOx layers resulted in a $-\Delta F$ of 34.1 ± 3.0 Hz (Δm of ≈603 ng cm^{-2}) and 206.6 ± 24.7 Hz (Δm of ≈3651 ng cm^{-2}) per layer, respectively.

It is important to note that the vertical assembly of the $(\text{Os-RM/GOx})_n$ multilayers was achieved through electrostatic interaction without crosslinking reaction. This preserves their inherent functional groups and facilitates robust enzyme immobilization. As evidenced by the ATR-FTIR spectra, the combined adsorption peaks from Os-RM and GOx consistently intensified as the bilayer number increased. This enhancement occurred

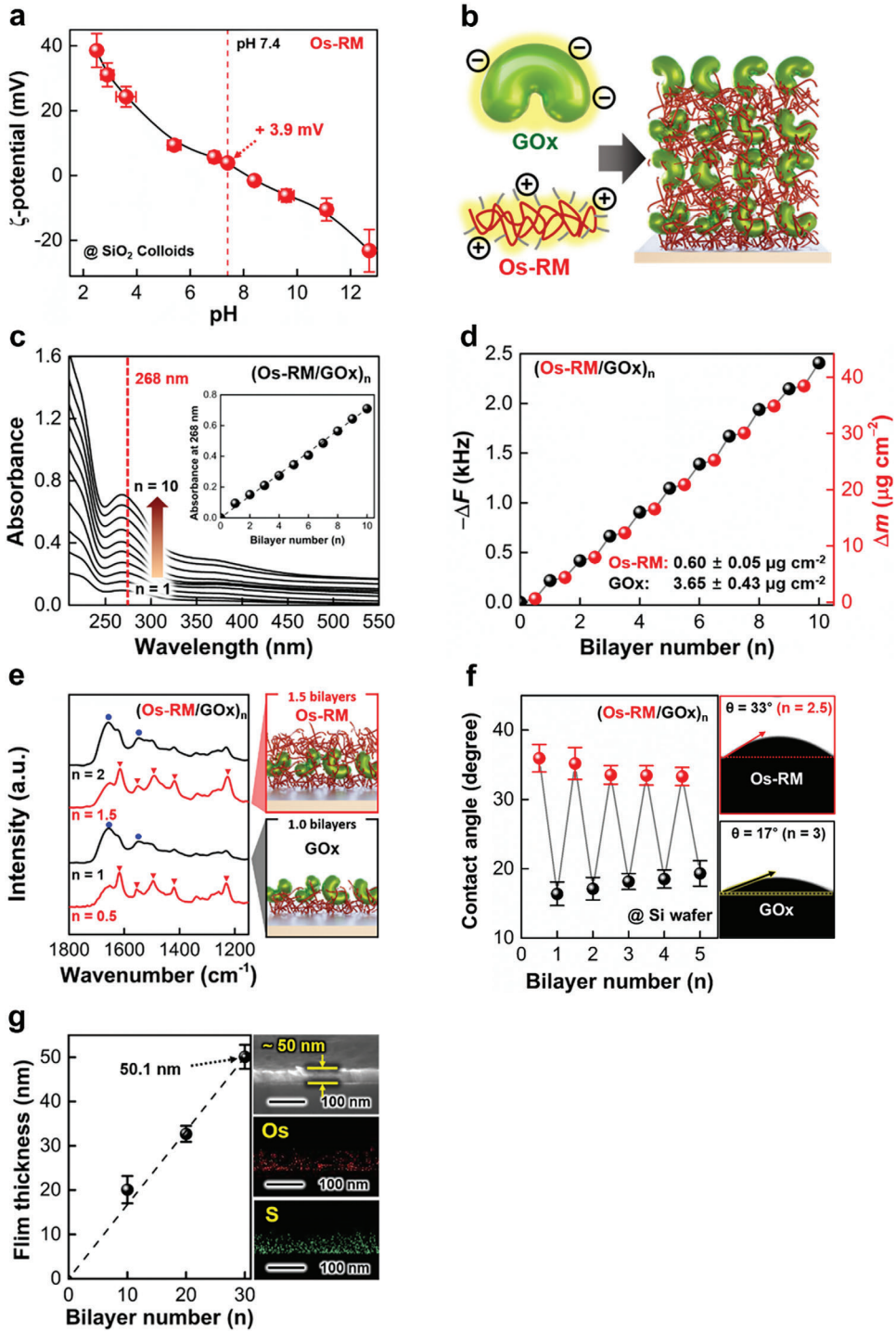

Figure 2. Characterization of $(Os\text{-}RM/GOx)_n$ multilayers. a) Change in Zeta potential values of Os-RMs as a function of aqueous solution pH. b) Schematic representation of electrostatic interaction-assembled $(Os\text{-}RM/GOx)_n$ multilayers. c) UV–vis absorbance spectra of $(Os\text{-}RM/GOx)_n$ multilayers with increasing bilayer number (n) from 1 to 10. The inset displays the absorbance measured at a wavelength of 268 nm, indicating linear growth of multilayers as a function of bilayer number. d) Frequency ($-\Delta F$) and mass change (Δm) of $(Os\text{-}RM/GOx)_n$ multilayers with increasing bilayer number (n) from QCM analysis. e) FTIR spectra of the $(Os\text{-}RM/GOx)_n$ multilayers with increasing bilayer number (n) from 0.5 to 2. f) Water contact angles (θ) measured from the $(Os\text{-}RM/GOx)_n$ multilayer-coated Au/Si-wafer. The top and bottom photographic images show the water droplets measured in cases where the outermost layer is Os-RM (i.e., $(Os\text{-}RM/GOx)_{n=2.5}$) and GOx (i.e., $(Os\text{-}RM/GOx)_{n=3}$), respectively. g) Film thicknesses of $(Os\text{-}RM/GOx)_n$ multilayers as a function of bilayer number (n) (left). Cross-sectional FE-SEM and energy-dispersive X-ray spectroscopy (EDS) elemental mapping images of the $(Os\text{-}RM/GOx)_n$ multilayer (n = 30) (right).

without the emergence of additional absorption peaks or the disappearance of intrinsic ones (Figure 2e; Figure S3, Supporting Information).

As opposed to simple mixed structures, a distinct characteristic of our LbL-assembled Os-RM/GOx multilayers is that they are integrated at the nanoscale level. To demonstrate this, we investigated the change in the water contact angles of $(Os\text{-}RM/GOx)_n$ films when the top surface layer was alternated between Os-RM and GOx. This process corresponded to odd and even layer numbers, respectively (Figure 2f). Water contact angle measurements are well known for their sensitivity to the chemical and physical properties of the top surface, with an effective range spanning just a few angstroms (Å).[36] For example, these measurements are significantly impacted by the chemical structure and the partial chain interdigitation present at the surface of sequentially adsorbed polyelectrolyte multilayers by complementary electrostatic interaction.[36–39] Based on this background, we extrapolated the physical and chemical characteristics of LbL-assembled (anionic GOx/cationic $Os\text{-}RM)_n$ multilayers, with a thickness of ≈1.67 nm per bilayer. Although the water contact angles of pure Os-RM and pure GOx single layers were measured to be about 42° and 13°, respectively, in our LbL assembled structures, the water contact angles of 34.3° and 17.9° were observed when the growth of the outermost layer was Os-RM and GOx terminated, respectively (Figure S4, Supporting Information). We attribute this discrepancy in the water contact angles to the interpenetration of Os-RM and GOx segments from previously adsorbed layers. Therefore, it is reasonable to conclude that the Os-RM/GOx multilayers exhibit significant nanoblending. More importantly, these results suggest the possibility that the electron transfer within the ultrathin Os-RM/GOx multilayers can be significantly enhanced compared to that within thick (> a few µm thick) and mechanically mixed films such as conventional slurry cast films. In the latter case, it should be noted that phase separation or segregation occurs between the RMs and enzymes due to thermodynamically unfavorable interfacial interactions that originate from large enthalpy penalties. The resultant macroscopically phase-separated structure makes electron transfer inefficient.[40]

Furthermore, we analyzed the film thickness of the LbL-assembled $(Os\text{-}RM/GOx)_n$ multilayers as the bilayer number (n) increased from 0 to 30. As illustrated in Figure 2g, the total film thickness reached ≈50 nm when n = 30, implying an approximate thickness of 1.67 nm per bilayer. Notably, energy-dispersive X-ray spectroscopy (EDS) images of the multilayers provided compelling evidence that Os atoms (attributed to RM) and sulfur atoms (associated with GOx) are highly dispersed within the multilayers. These observations corroborate our view that the densely nanoblended structures are formed in our LbL-assembled $(Os\text{-}RM/GOx)_n$ films.

2.2. Electrocatalytic Evaluation of Os-RM/Enzyme Multilayers

Based on these results, we aimed to create a high-performance MET-hybrid BFC anode using the $(Os\text{-}RM/GOx)_n$ multilayer assemblies. To achieve this goal, a highly conductive cotton fiber host electrode was developed. Structures comprised of (COOH-functionalized carbon nanotubes (C-CNTs) in ethanol/NH_2-functionalized tris(2-aminoethyl)amine (TREN) in ethanol)$_m$ multilayers (referred to as m-C-CNT multilayers, Figure S5, Supporting Information) and (tetra(octylammonium)bromide-stabilized Au NP (TOA-Au NP) in toluene/TREN in ethanol)$_n$ multilayers (referred to as n-Au NP) were deposited onto a 200 µm-thick cotton fiber (see Experimental section). The small molecular weight linker TREN ($M_w \approx 146$) used in this study significantly reduces the contact resistance between neighboring conductive CNTs as well as between Au NPs.[41,42] These phenomena are due to its ability to LbL assemble with C-CNTs via hydrogen bonding while simultaneously being able to LbL-assemble with the bare surface of Au NPs through a ligand exchange reaction (see Experimental Section). This transformation effectively converted the insulting cotton fiber into a highly conductive material. Our optimized conductive cotton fiber-based host electrode, denoted as the CCF host electrode, was composed of 10-C-CNT multilayers and 20-Au NP multilayers. This structure exhibits an impressive electrical conductivity of $\approx 8.5 \times 10^3$ S cm^{-1} and a low resistivity of $\approx 1.2 \times 10^{-4}$ Ω cm (**Figure 3a**). These electrical properties were found to depend on the bilayer number (m and n). It is important to note here that the CCF electrode retained the highly porous structure of pristine cotton fibers without any metal NP agglomeration, suggesting its capacity to accommodate substantial loading of Os-RM and GOx per unit area (Figure 3b).

Keeping this in mind, we deposited $(Os\text{-}RM/GOx)_n$ multilayers onto a negatively charged CCF host electrode for the formation of an anode (see Experimental Section), and subsequently investigated its electrochemical properties as a function of bilayer number (ranging from n = 0 to 7) and glucose concentration (from 0 to 300 mmol L^{-1}). A scan rate of 5 mV s^{-1} was maintained in a 20 mmol L^{-1} pH 7.4 phosphate-buffered saline (PBS) solution under ambient conditions (Figure 3c,d). Under a 300 mmol L^{-1} glucose concentration, the normalized anodic current density of the $(Os\text{-}RM/GOx)_n$/CCF electrode, measured at +0.6 V, reached a maximum value of 17.0 mA cm^{-2} (for n = 5), and then slightly decreased to 12.1 mA cm^{-2} for n = 7 (**Note**: when calculating the normalized anodic current density, we subtracted the background current density (at +0.6 V) of the $(Os\text{-}RM/GOx)_n$/CCF electrode at 0 mmol L^{-1} glucose from the current density measured at +0.6 V for the same electrode at 300 mmol L^{-1} glucose) (Figure 3c; Figures S6, and S7, Supporting Information). Although the Os-RM can shuttle electrons between the FAD centers of GOx and the host electrode via a ping-pong mechanism in an aqueous electrolyte solution, both the Os-RM and the GOx materials themselves have inherently poor electrical properties. Therefore, as the total thickness (or bilayer number) of the Os-RM/GOx multilayer structure is increased, it is possible that the total electron transfer efficiency of the anode can be significantly reduced. This implies that there should be an obvious trade-off between generated current density and multilayer film thickness in Os-RM/GOx-based anodes.[43] In our case, we find that the optimal thickness occurs in the $(Os\text{-}RM/GOx)_5$ multilayer structure, which has a thickness of ≈8.33 nm (see Figure 2g). Initially, when the bilayer number (n) is increased from 1 (thickness ≈1.67 nm) to 5 (thickness ≈8.33 nm), the increased amount of GOx in the structure generates more electrons, and then the Os-RM can effectively shuttle electrons from the GOx to the host electrode. However, as the bilayer number is further increased to 6 and 7, mass transfer and electron

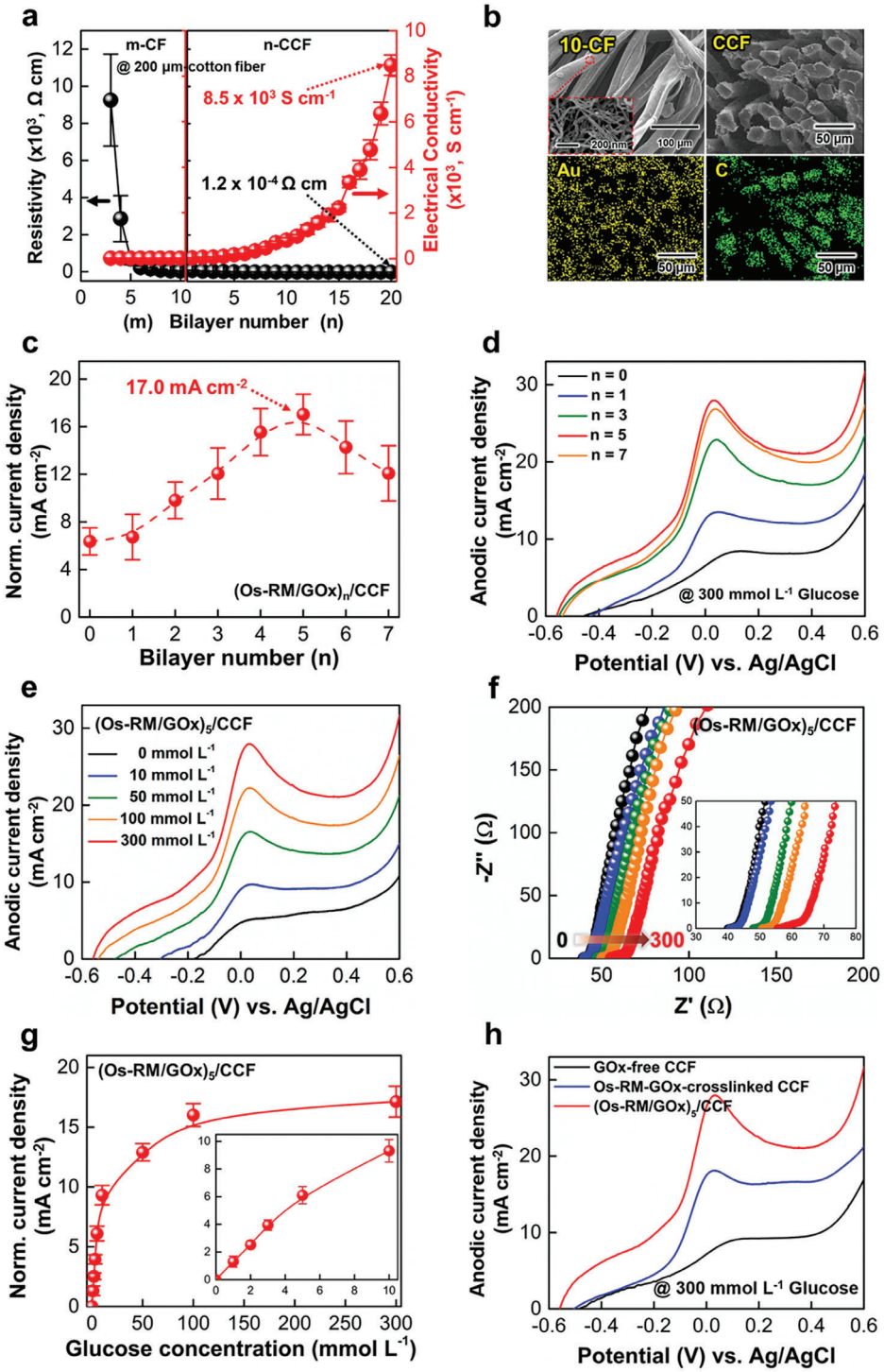

Figure 3. Electrochemical performance of $(Os\text{-}RM/GOx)_n$/CCF. a) Electrical conductivities of m-CF and n-CCF as a function of bilayer number (m and n). b) Planar and cross-sectional FE-SEM images (left top and right top images), along with EDS elemental mapping images of the 10-CF and CCF (bottom images). c) Dependence of the normalized current density on the bilayer number (n) of the $(Os\text{-}RM/GOx)_n$/CCF. d) Anodic current density curve of $(Os\text{-}RM/GOx)_n$/CCF with various bilayer number (n) at a scan rate of 5 mV s^{-1} in a PBS solution containing 300 mmol L^{-1} glucose at 36.5 °C. e) Anodic current density curves of $(Os\text{-}RM/GOx)_5$/CCF with increasing glucose concentration from 0 to 300 mmol L^{-1} (ordered from bottom to top). The glucose concentrations used are 0, 10, 50, 100, and 300 mmol L^{-1}, respectively. f) Nyquist plots of $(Os\text{-}RM/GOx)_5$/CCF with increasing glucose concentration from 0 to 300 mmol L^{-1}. g) Normalized current density of $(Os\text{-}RM/GOx)_5$/CCF with increasing glucose concentration from 0 to 300 mmol L^{-1} at +0.6 V and 36.5 °C. The inset shows the normalized current densities obtained from low glucose concentrations ranging from 0 to 10 mmol L^{-1}. h) Comparison of anodic current densities for three differently assembled CCFs: GOx-free CCF (black color), conventional Os-RM-GOx-crosslinked CCF (blue color), $(Os\text{-}RM/GOx)_5$/CCF (red color) at a scan rate of 5 mV s^{-1} in a PBS solution containing 300 mmol L^{-1} glucose.

generation is saturated at the surface and the total electron transfer efficiency starts to decrease within the multilayer-coated electrode, resulting in the decline of normalized anodic current density.

Additionally, we validated that the electrochemical anodic performance of the (Os-RM/GOx)$_5$/CCF electrode exhibited a strong correlation with glucose concentration. This correlation suggests that an increase in glucose concentration, ranging from 0 to 300 mmol L^{-1} (Figure 3e; Figure S8, Supporting Information), led to a higher rate of electrooxidation through the enzymes adsorbed on the electrode despite a slight increase of equivalent series resistance (ESR) from 40.5 to 56.1 Ω (Figure 3f). It should also be noted here that a more conductive CCF host electrode can generate a higher anodic current density in the (Os-RM/GOx)$_5$/CCF electrode, which can subsequently result in a higher power density hybrid BFC. For example, when 30-Au NP multilayers were deposited on the (C-CNT/TREN)$_{10}$/cotton fiber (i.e., (TOA-Au NP/TREN)$_{30}$/(C-CNT/TREN)$_{10}$/cotton fiber) instead of 20-Au NP multilayers, the resulting (Os-RM/GOx)$_5$/CCF electrode exhibited a higher electrical conductivity (conductivity ≈2.0×10^4 S cm^{-1} and a resistivity of ≈4.9×10^{-5} Ω cm for (TOA-Au NP/TREN)$_{30}$/(C-CNT/TREN)$_{10}$/cotton fiber) and anodic current density (Figure S9, Supporting Information). Considering that anodic current density is directly related to the power output of BFCs, these results suggest the possibility that the final power output of BFCs can be easily controlled by varying the bilayer number of Au NP multilayers in the host electrode. On a side note, we also demonstrated that the (Os-RM/GOx)$_5$/CCF anode exhibited a linear dependence of normalized current density at extremely low glucose concentrations ranging from 0 to 10 mmol L^{-1} (the inset of Figure 3g). These results evidently suggest the possibility that (Os-RM/GOx)$_n$/CCF electrodes could also be widely used as versatile in vivo glucose biosensors to monitor blood sugar levels for diagnosis and treatment of diabetes.[44]

Another significant observation we would like to point out is that the Au NPs incorporated within the CCF electrode catalyze the electrooxidation of glucose in aqueous electrolytes.[45] As already mentioned above, even in the case of a GOx-free CCF electrode, a background anodic current density corresponding to ≈53% of the anodic performance of the (Os-RM/GOx)$_5$/CCF electrode was exhibited in a 300 mmol L^{-1} glucose solution (Figure 3h; Figure S10, Supporting Information). This indicates that the highly porous CCF electrode can not only serve as a cocatalyst for glucose oxidation but also as a host electrode for the loading of GOx catalysts. Furthermore, the nanoblended (Os-RM/GOx)$_5$/CCF electrode with layered structure but seamless interfaces exhibited a superior anodic current performance compared to the Os-RM-GOx-crosslinked CCF electrode prepared using conventional slurry casting methods (see Figure 3h). These results demonstrate that the nanoblending LbL assembly between GOx and Os-RM increases the probability of close contact between the FAD center of GOx and the long active polymeric chains of Os-RMs, which is highly advantageous for electron transfer. Particularly, considering that the electrical conductivity of the LbL-assembled Os-RM/GOx multilayers themselves also has a substantial effect on the electron transfer between neighboring GOx species as well as between host electrode and multilayers, we cannot exclude the possibility that an increase in the electrical conductivity of Os-RM/GOx multilayers can further facilitate charge transfer and maximize the electrocatalytic reaction of the (Os-RM/GOx)$_n$/CCF electrode.

2.3. Electron Transfer-Intensified Os-RM/Enzyme Multilayer CCF Anodes

To evaluate such a possibility, we first investigated the interfacial interactions between Os-RMs and conductive metal NPs. Among various metal NPs, we selected TOA-Au NPs because of the possible existence of a high affinity (i.e., ligand exchange reaction between TOA ligands and Os-RM) between the imidazole groups of Os-RMs in a pH 7.4 PBS aqueous solution and TOA-Au NPs in toluene (**Figure 4a**). This affinity was examined by Fourier transform infrared (FTIR) spectroscopy. As shown in Figure 4b, as the bilayer number (n) of (Os-RM/TOA-Au NP)$_n$ multilayers was increased from 0.5 to 2, the apparent FTIR absorption peaks (C–H vibration of the imidazole rings of Os-RM at 3110 cm^{-1}) were strongly intensified (Figure S11, Supporting Information). This indicates the direct adsorption of Os-RMs onto the bare surface of Au NPs after the removal of pristine TOA ligands during sequential LbL assemblies (i.e., the C–H stretching peak at 2928 and 2856 cm^{-1}, originating from the long alkyl chain of bulky TOA ligands, disappeared when the Os-RM (n = 1.5) was deposited onto the TOA-Au NP-coated layer (n = 1.0)). Furthermore, the vertical growth of (Os-RM/TOA-Au NP)$_n$ multilayers was qualitatively and quantitatively confirmed by UV–Vis spectroscopy and QCM analyses, respectively. Specifically, Figure S12 (Supporting Information) shows the absorption spectra of bilayer number (n)-dependent (Os-RM/TOA-Au NP)$_n$ multilayers. As the bilayer number increases from 0 to 10, a regular increase is observed in the absorption peak intensity of Os-RM (at 263 nm) and the surface plasmon peak of TOA-Au NPs (at 550–600 nm). Additionally, as shown in Figure 4c, the loading amounts of Os-RM and TOA-Au NPs per bilayer were calculated to be ≈0.36 ± 0.07 and 1.61 ± 0.17 μg cm^{-2}, respectively.

Such reliable interfacial assembly behavior of the Os-RMs and TOA-Au NPs allows the systematic preparation of electron transfer-intensified (Os-RM/GOx/Os-RM/TOA-Au NP)$_p$ multilayers. The electrostatic interaction between Os-RM and GOx as well as the ligand exchange reaction-based covalent-bonding interaction between Os-RM and TOA-Au NPs play key roles in this process. Qualitatively similar to other LbL assemblies mentioned earlier, the total film thickness showed a regular increase according to the periodic number (p) of multilayers. Cross-sectional FE-SEM measurements showed that the total film thickness is 101 nm when p = 30, indicating a thickness of ≈3.3 nm per periodic layer (Figure 4d). Considering that the diameter of TOA-Au NPs is estimated to be about 7 nm, these data suggest that the surface coverage of TOA-Au NPs per periodic layer is insufficient in the lateral dimension. As such, a nanoblended internal structure should form within the multilayer films, which we confirm in EDS mapping images (see Figure 4d). It should also be noted here that despite the usage of toluene and other aqueous solutions in the synthesis process, no residual organic solvent was detected in the (Os-RM/GOx/Os-RM/TOA-Au NP)$_3$/CCF anode after a sufficient drying process (Figure S13, Supporting Information).

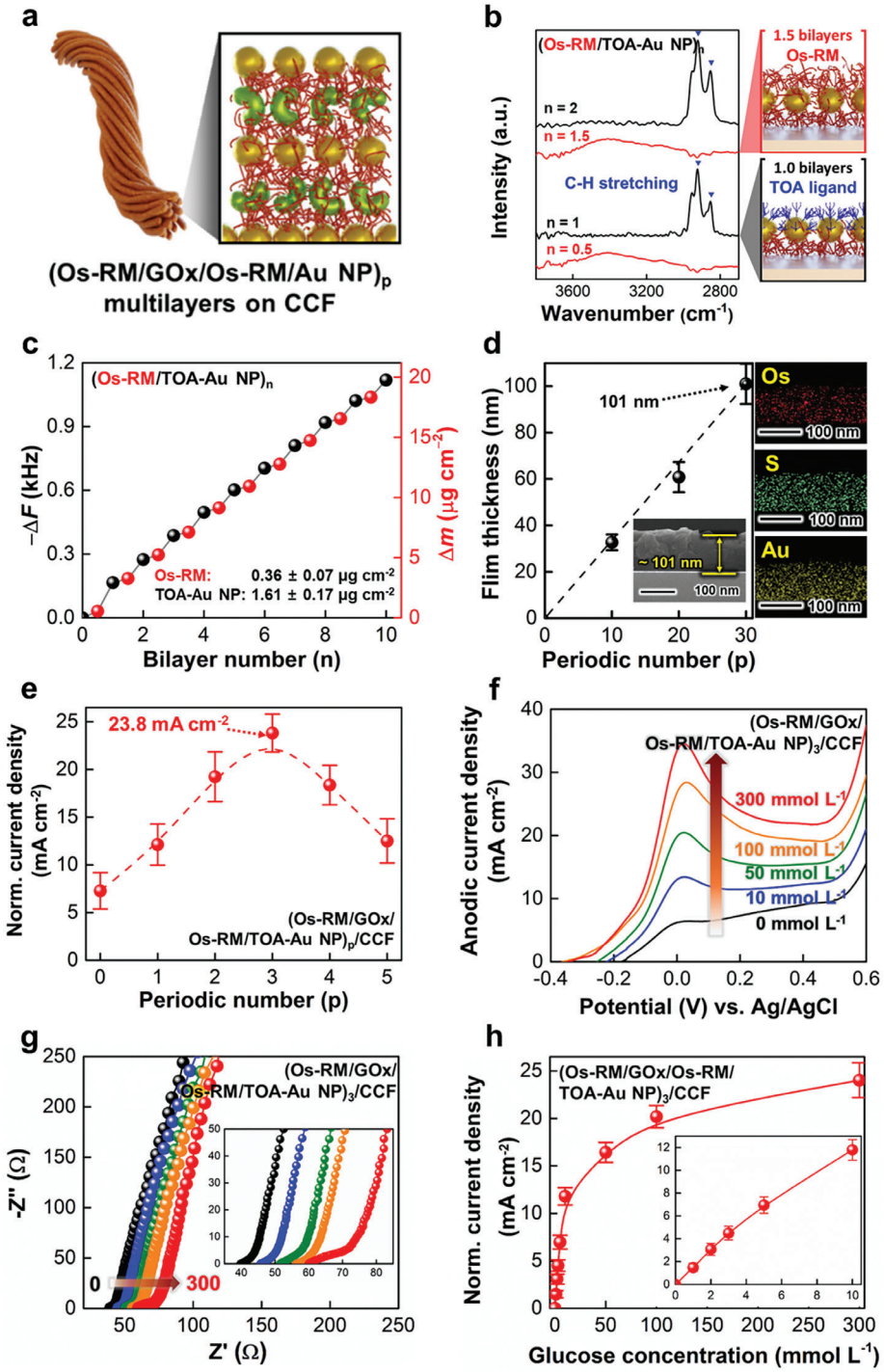

Figure 4. Characterization of (Os-RM/GOx/Os-RM/TOA-Au NP)$_p$ multilayers and their anodic performance on CCF electrode. a) Schematic illustration of (Os-RM/GOx/Os-RM/TOA-Au NP)$_p$ multilayers. b) FTIR spectra of the (Os-RM/TOA-Au NP)$_n$ multilayers as a function of bilayer number (n). c) Frequency ($-\Delta F$) and mass change (Δm) in the QCM data of (Os-RM/TOA-Au NP)$_n$ multilayers with increasing bilayer number (n) from 0 to 10. d) Thickness of the (Os-RM/GOx/Os-RM/TOA-Au NP)$_p$ multilayer as a function of periodic number (p) (left) and cross-sectional FE-SEM images (inset). The EDS elemental mapping images of (Os-RM/GOx/Os-RM/TOA-Au NP)$_{30}$ multilayers grown on a Si wafer are shown on the right. e) Dependence of the normalized current density on the periodic number (p) of the (Os-RM/GOx/Os-RM/TOA-Au NP)$_p$/CCF. f) Anodic current density curves of (Os-RM/GOx/Os-RM/TOA-Au NP)$_3$/CCF with increasing glucose concentration from 0 to 300 mmol L^{-1} at 36.5 °C (ordered from bottom to top). The glucose concentrations used are 0, 10, 50, 100, and 300 mmol L^{-1}, respectively. g) Nyquist plots of (Os-RM/GOx/Os-RM/TOA-Au NP)$_3$/CCF with increasing concentration of glucose from 0 to 300 mmol L^{-1}. h) Normalized current density of (Os-RM/GOx/Os-RM/TOA-Au NP)$_3$/CCF with increasing glucose concentration from 0 to 300 mmol L^{-1} at +0.6 V and 36.5 °C. The inset shows the normalized current densities obtained from low glucose concentrations ranging from 0 to 10 mmol L^{-1}.

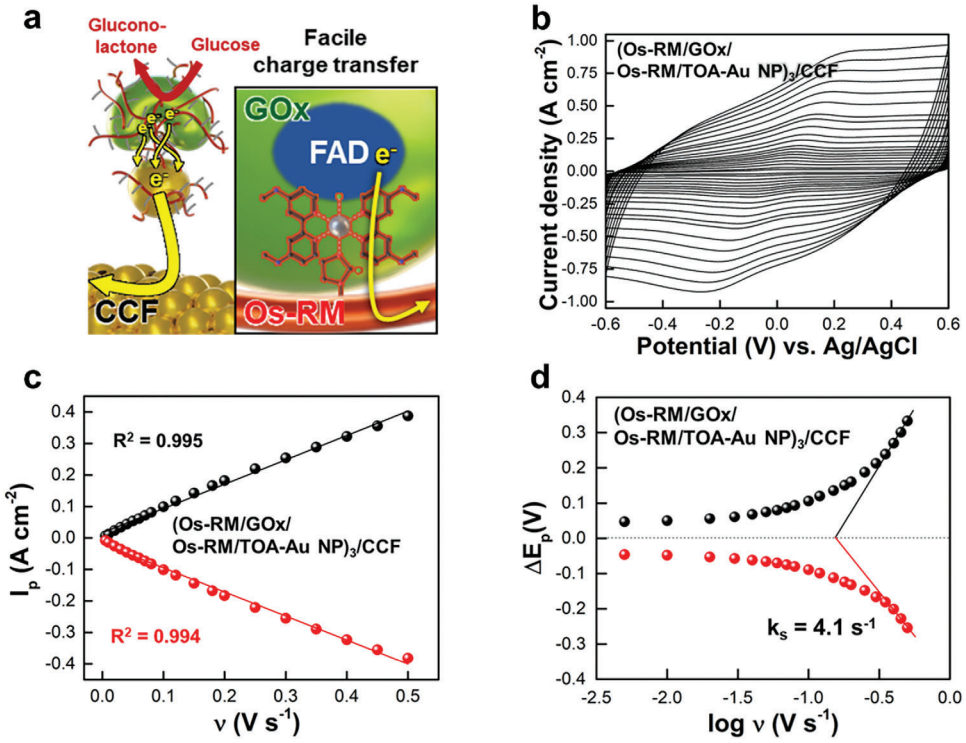

Figure 5. Electron transfer mechanism of anodes based on Os-RM/GOx/Os-RM/TOA-Au NP multilayers. a) Schematic illustration depicting electron transfer in the Os-RM/GOx/Os-RM/TOA-Au NP/CCF system. b) Scan rate-dependent cyclic voltammograms (CVs) of (Os-RM/GOx/Os-RM/TOA-Au NP)$_3$/CCF in the PBS buffer solution. In this case, scan rates ranging from 0.005 V s^{-1} (the inner curve) to 0.5 V s^{-1} (the outer curve) were used for electrochemical measurements. The scan rates used were 0.005, 0.01, 0.02, 0.03, 0.04, 0.05, 0.06, 0.07, 0.08, 0.1, 0.12, 0.15, 0.18, 0.2, 0.25, 0.3, 0.35, 0.4, 0.45, 0.5 V s^{-1}, respectively. c) Change in the peak current densities of the (Os-RM/GOx/Os-RM/TOA-Au NP)$_3$/CCF with increasing scan rate (ν) from 0.005 to 0.5 V s^{-1}. d) Electrochemical response of the (Os-RM/GOx/Os-RM/TOA-Au NP)$_3$/CCF. Change in the potential ($E-E_0$) of (Os-RM/GOx/Os-RM/TOA-Au NP)$_3$/CCF as a function of log (ν). In this case, the (Os-RM/GOx/Os-RM/TOA-Au NP)$_3$/CCF exhibited a remarkably high k_s value of ≈4.1 s^{-1}.

Based on these results, we investigated the electrochemical performance of the (Os-RM/GOx/Os-RM/TOA-Au NP)$_p$ multilayer-coated CCF anode as a function of periodic layer number (p) (Figure 4e; Figure S14, Supporting Information). Under a fixed glucose concentration of 300 mmol L^{-1}, the normalized current density significantly increased from 7.3 to 23.8 mA cm^{-2} as the periodic layer number increased up to p = 3 and then subsequently decreased to 12.5 mA cm^{-2} for p = 5. Therefore, for the preparation of a high-performance (Os-RM/GOx/Os-RM/TOA-Au NP)$_p$/CCF anode, the optimized periodic layer number was determined to be p = 3. The maximum anodic current densities at +0.6 V in the glucose concentrations of 10 and 300 mmol L^{-1} were measured to be ≈21.1 and 37.5 mA cm^{-2}, respectively (Figure 4f; Figures S14–S16, Supporting Information). This electrochemical activity of the (Os-RM/GOx/Os-RM/TOA-Au NP)$_p$ multilayer-coated CCF anode was also confirmed to be mechanically stable (Figure S17, Supporting Information). On the other hand, when the glucose concentration was increased from 0 to 300 mmol L^{-1}, the ESR values of the (Os-RM/GOx/Os-RM/TOA-Au NP)$_3$/CCF anode only slightly increased from ≈42.1 to 60.9 Ω (Figure 4g; Figure S15, Supporting Information). This trend is almost identical to what was observed for the (Os-RM/GOx)$_5$ multilayer anode (see Figure 3f). Given that the total film thickness of the (Os-RM/GOx/Os-RM/TOA-Au NP)$_3$ multilayers (≈10 nm) was thicker than that of the (Os-RM/GOx)$_5$ multilayers (≈8.3 nm), the similar ESR values imply that the incorporation of metal NPs has an important effect on the electron transfer characteristics of Os-RM-based anodes. Particularly, it's worth noting that compared to its metal NP-free counterpart, the normalized anodic current densities of the (Os-RM/GOx/Os-RM/TOA-Au NP)$_3$/CCF measured at +0.6 V increased to ≈24 mA cm^{-2} (at 300 mmol L^{-1} glucose) while maintaining Michaelis–Menten-type behavior (i.e., saturation after a linear dependence in normalized current density as a function of glucose concentration) (Figure 4h). These results clearly show that the electrooxidation reaction of the (Os-RM/GOx/Os-RM/TOA-Au NP)$_3$/CCF has a much higher efficiency than that of the (Os-RM/GOx)$_5$/CCF.

Furthermore, we investigated the electron transfer kinetics of the TOA-Au NP-incorporated anode [i.e., (Os-RM/GOx/Os-RM/TOA-Au NP)$_3$/CCF)] using the Laviron model (**Figure 5a–d**).[46] The anodic and cathodic peak currents of the TOA-Au NP-incorporated anode increased linearly with the scan rate (see Figure 5b,c). This implies that the electron transfer reaction of the anode is quasireversible and surface controlled, providing a constant charge value independent of scan rate. In addition, the apparent heterogeneous electron transfer rate constant (k_s) of the (Os-RM/GOx/Os-RM/TOA-Au

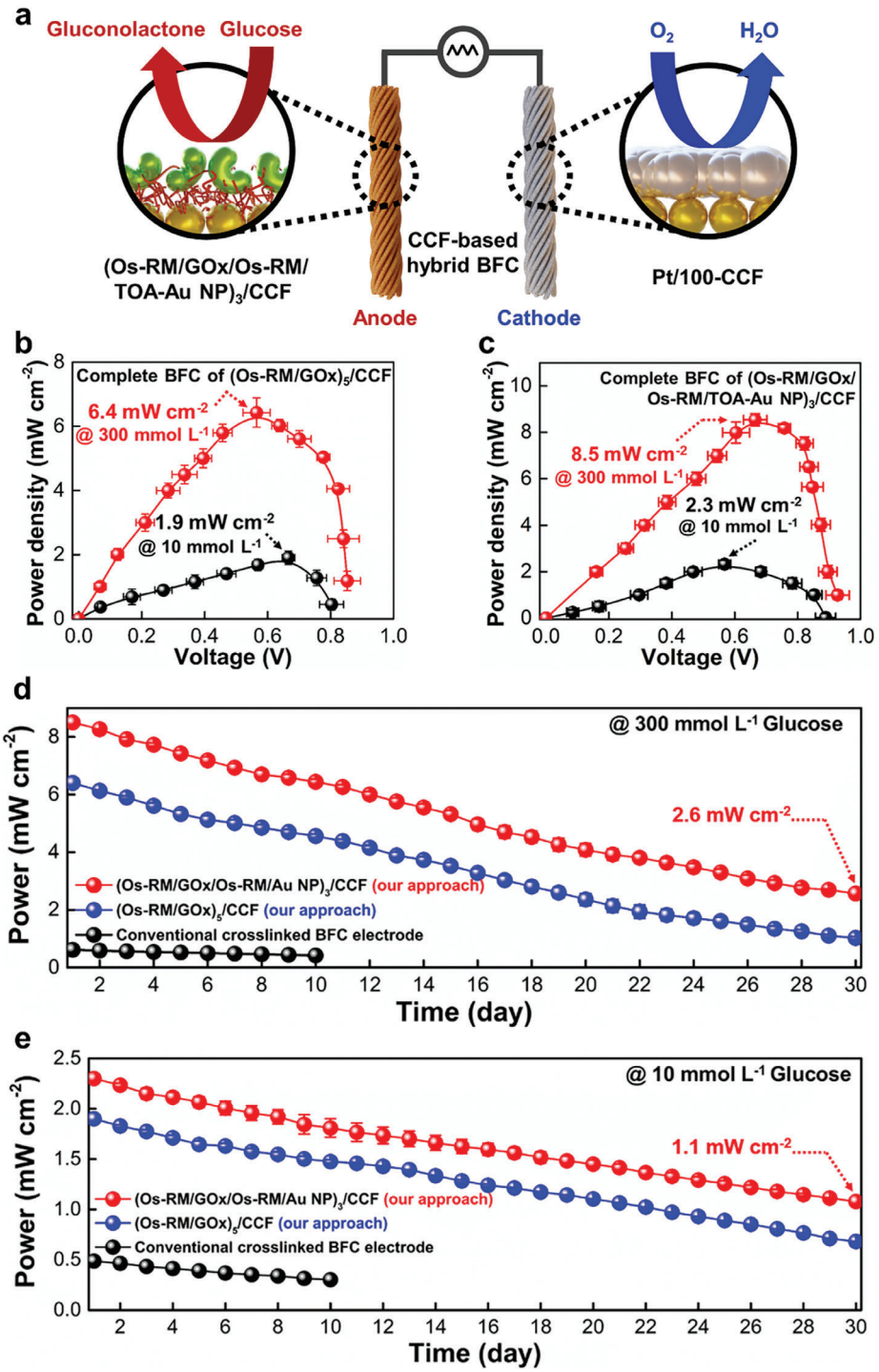

Figure 6. Performance of prototype hybrid BFC utilizing CCF electrodes. a) Schematic illustration of prototype hybrid BFCs operating in a glucose-containing buffer solution. b) Power output of prototype hybrid BFCs composed of a (Os-RM/GOx)$_5$/CCF anode and a Pt/(TOA-Au NP/TREN)$_{100}$/(C-CNT/TREN)$_{10}$/cotton fiber cathode. The power output was measured in a PBS solution containing 10 mmol L^{-1} (black color) and 300 mmol L^{-1} (red color) glucose under ambient conditions at 36.5 °C. The cell potential was controlled by adjusting the current through external variable resistors (ranging from 1 kΩ to 10 MΩ). c) Power output of prototype hybrid BFCs composed of (Os-RM/GOx/Os-RM/TOA-Au NP)$_3$/CCF anodes and Pt/(TOA-Au NP/TREN)$_{100}$/(C-CNT/TREN)$_{10}$/cotton fiber cathodes in PBS solutions containing 10 and 300 mmol L^{-1} glucose at 36.5 °C. d) Power retention of prototype hybrid BFCs comprised of conventional crosslinked electrodes (black color), (Os-RM/GOx)$_5$/CCFs (blue color, our approach), and (Os-RM/GOx/Os-RM/TOA-Au NP)$_3$/CCFs (red color, our approach) in PBS solutions containing 300 mmol L^{-1} glucose at 36.5 °C. e) Power retention of prototype hybrid BFCs comprised of conventional crosslinked BFC electrode (black color), (Os-RM/GOx)$_5$/CCFs (blue color, our approach), and (Os-RM/GOx/Os-RM/TOA-Au NP)$_3$/CCFs (red color, our approach) in PBS solutions containing 10 mmol L^{-1} glucose at 36.5 °C. In all cases, a Pt/(TOA-Au NP/TREN)$_{100}$/(C-CNT/TREN)$_{10}$/cotton fiber cathode was used.

NP)$_3$/CCF was calculated to be ≈4.1 s^{-1} (see Figure 5d and Experimental Section). This notably high k_s value of the electron transfer-intensified anode suggests that our anode has a rapid heterogeneous electron transfer process, mainly due to the efficient redox reaction between the GOx and the host electrode thanks to the intercalation of TOA-Au NPs between adjacent Os-RMs.

To further confirm the contribution of TOA-Au NPs to the improvement of electron transfer kinetics in the GOx, we examined the electron transfer rate constants of the (Os-RM/GOx)$_5$/CCF anode in the absence of TOA-Au NPs. In this case, the k_s value was estimated to be ≈3.0 s^{-1} (Figure S18, Supporting Information), which still outperformed that of (Os-RM-GOx)-crosslinked CCF obtained from the conventional slurry-casting method (k_s ≈1.7 s^{-1}, see Figure S19, Supporting Information). Even in electrodes without the TOA-Au NPs, this relatively high k_s value of the LbL-assembled (Os-RM/GOx)$_5$/CCF anode implies that the seamless interfaces formed by the LbL assembly establish an efficient electron transfer route between Os-RM and GOx.

2.4. Performance of Complete Hybrid BFCs Utilizing Electron Transfer-Intensified Anodes

Following the promising results of our electron transfer-intensified anode, we proceeded to fabricate a prototype hybrid BFC and assessed its performance. In our cells, we chose to use a (TOA-Au NP/TREN)$_{20}$/(C-CNT/TREN)$_{10}$/cotton fiber as the cathode because of the high and stable oxygen reduction reaction (ORR) activity exhibited by Au NPs.[47] Although various enzymes, such as laccase or bilirubin oxidase, can serve as cathodic enzymes due to their ORR activity,[48–50] it is important to note that their catalytic activity and operational stability are highly dependent on physiological conditions, such as pH, temperature, and chlorine concentration, which are specific to living organisms, including humans. Moreover, their ORR activity and stability lag behind those of Au NPs and Pt.[48,51,52]

To further enhance the ORR activity of the CCF-based cathode, we increased the bilayer number of TOA-Au NP/TREN multilayers from 20 to 100. Additionally, we sputtered Pt on top of the multilayers as it is known for its superior ORR activity compared to Au.[52,53] As a result, we obtained a Pt/(TOA-Au NP/TREN)$_{100}$/(C-CNT/TREN)$_{10}$/cotton fiber electrode (hereafter Pt-CCF), which exhibited significantly enhanced cathodic activity compared to the pristine CCF electrode (see Experimental section and Figure S20, Supporting Information). Furthermore, it is worth noting that the oxygen reduction reaction (ORR) at the cathode can be enhanced by increasing the bilayer number of TOA-Au NP/TREN multilayers on Pt-CCF from 100 to 130 (Figure S21, Supporting Information), and on the other hand, the maximum power output of the full-cell hybrid BFC is almost saturated due to the limited performance of anode. Implementing this optimized cathode, we investigated the power output of hybrid BFCs featuring MET anode configurations with and without the incorporated TOA-Au NPs (see Experimental Section, **Figure 6**a; Figure S22, Supporting Information). Here, the power density was evaluated by measuring the current flow across a fixed external resistance in the range of 1 kΩ to 10 MΩ (Figure 6b,c; Figures S23 and S24, Supporting Information). In the hybrid BFC using a simple (Os-RM/GOx)$_5$ multilayered anode, high power outputs of ≈1.9 and 6.4 mW cm^{-2} were observed when operating with glucose concentrations of 10 and 300 mmol L^{-1}, respectively. It is worth noting that the significant areal power output of 1.9 mW cm^{-2} even at the low glucose concentration of 10 mmol L^{-1} makes this setup particularly suitable for a wide range of biomedical applications.[28,54,55] Intriguingly, this performance could be further enhanced by utilizing our electron transfer-intensified MET anode. Specifically, a fully assembled hybrid BFC device composed of a (Os-RM/GOx/Os-RM/TOA-Au NP)$_3$ anode and a Pt/(TOA-Au NP/TREN)$_{100}$/(C-CNT/TREN)$_{10}$/cotton fiber cathode displayed record-high power outputs. At glucose concentrations of 10 and 300 mmol L^{-1}, it delivered remarkable power densities of 2.3 and 8.5 mW cm^{-2}, respectively, along with a considerably high open-circuit voltage of 0.92 V. These values represent a monumental leap forward compared to previously reported single fibrous MET-BFCs (Table S1, Supporting Information). Moreover, the hybrid BFCs exhibited outstanding operational stability. After 10 days of continuous operation, they retained ≈80% (1.8 mW cm^{-2} at glucose concentration of 10 mmol L^{-1}) of their initial power density, and this value decreased to only 47% (1.1 mW cm^{-2}) even after 30 days. These stability values are significantly higher than those observed for systems without TOA-Au NPs (Figure 6d,e), as well as conventional MET-BFCs based on crosslinked Os-RM/GOx slurries (Figure S25, Supporting Information). Additionally, to confirm the repeatability of our process and the experimental consistency of hybrid BFC performance, we prepared three different hybrid BFCs, each comprised of a separate (Os-RM/GOx/Os-RM/TOA-Au NP)$_3$/CCF anode and a common Pt/(TOA-Au NP/TREN)$_{100}$/(C-CNT/TREN)$_{10}$/cotton fiber cathode. No significant disparities were observed in the power output characteristics of the three samples (Figure S26, Supporting Information).

Collectively, our results demonstrate a substantial advancement in electron mediation and enzyme immobilization within hybrid BFC electrodes. This was primarily realized thanks to prudent design of interfacial interactions, with an emphasis on the assembly of metal NP-linked Os-RMs and enzymes, which allowed the fabrication of electron transfer-intensified anode structures.

3. Conclusion

In this study, we successfully demonstrated that a high-performance hybrid BFC could be prepared using electron transfer-intensified mediator layers and a multi-interaction-based interfacial assembly approach. Our assembly method is characterized by its ability to seamlessly nanoblend and integrate all components within the host electrode, cathode, and anode onto a fibril-structured substrate through complementary interactions, resulting in the formation of all-in-one structured electrodes with uninterrupted interfaces. A particularly noteworthy aspect of our approach is the robust and seamless interfacial assembly of Au NPs between adjacent Os-RM layers. This elegant arrangement significantly enhances electron transfer from the Os-RM to the GOx without requiring the synthesis of complex, unconventional RM materials. When our high-performance anode was combined with a Pt-sputtered cathode, the prototype

MET-hybrid BFC exhibited a record-high areal power output of ≈8.5 mW cm^{-2} (at glucose concentration of 300 mmol L^{-1}) with remarkable operational stability (47% of initial power density after one month), which significantly outperformed previously reported MET-BFCs. Particularly, considering that our approach is closely related to the improvement of electron transfer kinetics, interfacial interactions, structural design, and electrochemical performance, we believe that our approach can also provide a basis for developing and designing a variety of other high-performance electrochemical devices as well.

4. Experimental Section

Materials: Cotton fibers with a diameter of 200 µm were purchased from Igonji, multi-walled carbon nanotubes (MWCNTs with a diameter of 7 to 9 nm, a length of 10 to 50 µm, and a purity of more than 80%) were purchased from Nanosolution Co. Ltd (South Korea). A MWCNT fiber substrate with a diameter of ≈35 µm was purchased from Taiyo Nissan and used for conventional crosslinked BFC electrode. Glucose oxidase (GOx) from Aspergillus niger (236 U mg^{-1}) was purchased from Amano Enzyme Inc. (Japan). Tetraoctylammonium bromide (TOA), gold(III) chloride trihydrate ($HAuCl_4 \cdot 3H_2O$), sodium borohydride ($NaBH_4$), tris-(2-aminoethyl)amine (TREN), polyethyleneimine, branched (PEI, M_w ≈ 800 g mol^{-1}), tricarballylic acid (TC), ammonium hexachloroosmate (IV) (reagent grade), 4,4′-dimethoxy-2,2′-bipyridine (dmo–bpy, 97%), 1-vinylimidazole (99%), ethyl acetate (anhydrous, 99.8%), ethylene glycol (anhydrous, 99.8%), and ethanol (absolute grade for synthesis and anhydrous grade for precipitation) were purchased from Sigma–Aldrich Co. (Milwaukee, WI, USA). Azobisisobutyronitrile (AIBN, EP, 99%) and diethyl ether (GR, 99.5%) were purchased from Daejung Chem Co. (South Korea) The analytical reagents were used without further purification. Potassium dihydrogen phosphate (KH_2PO_4), sodium hydrogen phosphate (Na_2HPO_4), sodium chloride (NaCl), potassium chloride (KCl), and all other solutions were prepared using deionized (DI) Milli-Q water (Millipore, Tokyo, Japan). Microparticles GmbH, SiO_2-R-0.5 (Silica Company, Germany) was used as the particulate material in this study. These particles are white, natural crystalline silica powders with a size of 0.56 µm (SD: 0.02 µm).

Synthesis of C-CNT: Carboxylic acid-functionalized MWCNTs (C-CNTs) were prepared by subjecting pristine MWCNTs to a strong acid treatment using H_2SO_4/HNO_3 at 75 °C for 2.5 h. The resulting C-CNTs were purified by centrifugation and vacuum filtration to remove the residual acid. The prepared C-CNTs were redispersed in ethanol.

Synthesis of TOA-Au NPs: TOA-stabilized Au NPs (TOA-Au NPs) with a diameter of 8 nm were synthesized by a two-phase method in toluene.[56] Initially, $HAuCl_4 \cdot 3H_2O$ in deionized water (30 mmol L^{-1}, 30 mL) and TOA stabilizers in toluene (20 mmol L^{-1}, 80 mL) were vigorously stirred together. Subsequently, $NaBH_4$ solution in water (400 mmol L^{-1}, 25 mL) was added to the two-phase mixture. After stirring for ≈2.5 h, the aqueous phase was separated, and the remaining toluene solution was repeatedly washed with dilute aqueous H_2SO_4 (100 mmol L^{-1}), NaOH (100 mmol L^{-1}), and deionized water. Finally, following several washing steps and the removal of the aqueous solution, a suspension of TOA-Au NPs dispersed in toluene was obtained.

Synthesis of PVI: Poly(1-vinylimidazole) (PVI) was synthesized in a round-bottomed flask by dissolving 1-vinylimidazole (36.8 mmol) in ethyl acetate (30.0 g) under reflux with stirring at 120 rpm at 30 °C. A solution of azobisisobutyronitrile (AIBN, 0.368 mmol) dissolved in ethyl acetate (5.0 g) was slowly added dropwise under nitrogen purging at 70 °C for 1 day. Following the reaction, the solution was reprecipitated in 5.0 L of diethyl ether and subsequently filtered through a 0.45 µm nylon filter. Finally, the product was dried under vacuum at 60 °C for 1 day prior to use.[23]

Synthesis of $Os(dmo–bpy)_2Cl_2$: $Os(dmo–bpy)_2Cl_2$ was synthesized following a previously reported procedure.[19] Ammonium hexachloroosmate (2.28 mmol) and dmo-bpy (5.02 mmol) were stirred and refluxed in a round-bottomed flask containing 100 mL of ethylene glycol at 180 °C for 1 h. After the reaction, sodium hydrosulfite (91.2 mmol) dissolved in 350 mL of deionized water was added to the product mixture. This mixture was refrigerated at 4 °C for 15 min. The reduced product was then collected by vacuum filtration through a nylon filter. The final product was obtained after drying completely in an oven at 40 °C for 2 days.

Synthesis of PVI–$[Os(dmo–bpy)_2Cl]^{+/2+}$ (Os-RM): PVI–$[Os(dmo–bpy)_2Cl]^{+/2+}$ was synthesized following a previously reported procedure.[57] PVI polymer powder (0.474 g, 7 eq) and $Os(dmo–bpy)_2Cl_2$ (0.5 g, 1 eq) were stirred under reflux in a jacketed reaction flask containing 500 mL of ethanol under a nitrogen atmosphere at 120 °C for 12 h. After the reaction, the solution was slowly added dropwise to 5,000 mL of diethyl ether to precipitate the product. The precipitate was then dissolved in 400 mL of deionized water. The resulting solution was concentrated using ultrafiltration discs with a 10 kDa molecular weight cut-off. Subsequently, the concentrated solution was precipitated by dropwise addition to 2000 mL of diethyl ether. The precipitate was then redissolved in 50 mL of ethanol. This process of dissolving the precipitate in ethanol followed by reprecipitation in diethyl ether was repeated once to ensure the complete purification. Finally, the precipitate was filtered using a 0.45 µm nylon filter, and then dried under vacuum at 60 °C for 1 day.[20,23,57]

Preparation of $(C\text{-}CNT/TREN)_n$/Cotton Fiber: Cotton fibers, comprised of cellulose featuring hydroxyl (OH) groups, were immersed in a 1 mg mL^{-1} ethanol solution of amine (NH_2)-functionalized poly(ethylene imine) (PEI) with a molecular weight of ≈800 for 2 h. This process led to the formation of a PEI coating on the fibers through hydrogen bonding interactions between the NH_2 groups of PEI and the OH groups of cellulose. In particular, it should be noted that these PEI polymers have much larger amounts of NH_2 groups than small TREN molecular linkers, which is highly advantageous for the conversion of OH-functionalized cotton fibers from NH_2-functionalized cotton fibers.

Next, the PEI-coated fibers were dipped in a C-CNT solution for 10 min and then washed with pure ethanol to remove weakly adsorbed C-CNT. Subsequently, the C-CNT-coated fibers were immersed in a 2 mg mL^{-1} ethanol solution of TREN for 10 min and rinsed with pure ethanol. This allowed the carboxyl group of C-CNT to bind with the NH_2 group of TREN via hydrogen bonding, resulting in fibers coated with one bilayer (i.e., $(C\text{-}CNT/TREN)_1$/cotton fiber). The deposition of (C-CNT/TREN) was repeated 10 times to create a $(C\text{-}CNT/TREN)_{10}$ coating onto the cotton fibers (i.e., 10-CF), yielding an electrical conductivity of ≈0.05 S cm^{-1}.

Preparation of CCF Electrode: A conductive cotton fiber electrode (i.e., the outermost TREN layer-coated CF) was prepared by immersing 10-CF in a 5 mg mL^{-1} solution of TOA-Au NPs for 40 min, followed by washing with toluene to remove weakly adsorbed nanoparticles. After this adsorption process, the bulky TOA ligands loosely bound to the Au NP surface were almost completely replaced by the NH_2 groups of TREN due to the strong affinity between Au and NH_2 groups. Subsequently, the TOA-Au NP-coated fibers were immersed in a 2 mg mL^{-1} solution of TREN in ethanol for 10 min. These deposition and washing steps were repeated until the desired number of bilayers was achieved. The resulting electrode was the outermost TREN layer-coated CCF, which was positively charged in pH 7.4 PBS solution due to the conversion from neutral amine (NH_2) (in ethanol) to positively charged amine (NH_3^+).

Preparation of $(Os\text{-}RM/GOx)_n$/CCF Anode: For the preparation of $(Os\text{-}RM/GOx)_n$ multilayers, the outermost TREN layer-coated CCF electrode with positive charges was additionally functionalized with negatively charged tricarballylic acid (TC) for 20 min in a 1 mg mL^{-1} aqueous solution. After thorough rinsing, the TC-modified electrode was immersed in a 4 mg mL^{-1} solution of positively charged Os-RM in PBS (pH 7.4) for 10 min and washed again. This facilitated the formation of stable deposition through electrostatic interactions between the carboxyl groups of TC and the amine groups of Os-RM. Subsequently, this process was repeated with negatively charged GOx (5 mg mL^{-1} in PBS with 500 mmol L^{-1} NaCl, pH 7.4) using the same deposition time (10 min) and another layer of positively charged Os-RM, each followed by thorough washing to remove weakly bound molecules. The deposition and washing cycle was repeated

until the desired bilayer number was achieved for the formation of the (Os-RM/GOx)$_n$ multilayers.

Preparation of (Os-RM/GOx/Os-RM/TOA-Au NP)$_p$/CCF Anode: The outermost TREN layer-coated CCF electrode with positive charges was additionally functionalized with negatively charged tricarballylic acid (TC) for 20 min in a 1 mg mL^{-1} aqueous solution. Following thorough rinsing, the TC-modified electrode was immersed in a 4 mg mL^{-1} solution of positively charged Os-RM in PBS (pH 7.4) for 10 min and washed again. This step allowed electrostatic interactions between the carboxyl groups of TC and the amine groups of Os-RM to form a stable deposition. The process was repeated with negatively charged GOx (5 mg mL^{-1} in PBS with 500 mmol L^{-1} NaCl, pH 7.4) and another layer of positively charged Os-RM, each followed by thorough washing to remove weakly bound molecules. Finally, the electrode was immersed in a TOA-Au NP solution for 10 min and washed with toluene. In this case, TOA-Au NPs were deposited onto the outermost Os-RM layer-coated CCF electrode via a ligand exchange reaction between TOA ligands bound to the surface of Au NPs and amine groups of Os-RM. This multi-step deposition and washing sequence was repeated until the desired number of layers was achieved.

Preparation of Conventional Os-RM/GOx-Crosslinked Slurry: To prepare the conventional Os-RM/GOx crosslinked slurry for anodes, enzymes, redox mediators, and crosslinking agents were uniformly mixed and used without precipitation. The anodic catalyst consists of the crosslinking adducts of GOx (41 wt%), Os-RM (52 wt%), and PEGDGE (7 wt%). The optimal crosslinking agent concentration was determined based on both the current density output and the stability of the BFC electrodes according to the previously reported procedure.[6] Both the conventional crosslinked CNT electrodes and CCF electrodes were absorbed into the optimized slurry at 4 °C for 24 h and finally cured at 4 °C for 24 h.

Preparation of Cathode: To prepare the cathode for BFCs, a vacuum sputtering process was used to deposit Pt onto the outermost TREN layer-coated CCF electrode. This process utilized an ion sputter coater (MC1000, Hitachi) with argon (Ar) gas flow, and a discharge current of 20 mA. The duration of sputtering was adjusted, with a maximum sputtering time of 90 s.

Characterization and Analysis of CCF Electrode: The surface and cross-sectional morphologies of the CCF-based BFCs electrodes were characterized using FE-SEM (Hitachi S4800, Japan). The adsorption behavior and mechanism of formation of the (Os-RM/GOx)$_n$, (Os-RM/TOA-Au NP)$_n$ multilayers were investigated using FT-IR spectroscopy in specular mode. The growth and loading amount of the LbL-assembled multilayers were examined using UV–Vis spectroscopy on quartz glass, and a QCM (QCM 200, SRS, USA), respectively. In the case of QCM measurement, the mass change (ΔM) per layer was calculated from the QCM frequency change (ΔF) using the Sauerbrey equation,[32,33]

$$\Delta F\ (Hz) = -\frac{2F_0^2}{A\sqrt{\rho_q \mu_q}} \cdot \Delta M \tag{1}$$

where F_0, A, ρ_q, and μ_q represent the resonant frequency (≈5 MHz), the active area (cm^2), the density (2.65 g cm^{-3}), and the shear modulus (2.95×10^{11} g cm^{-1} s^{-2}) of the QCM electrode, respectively. This expression can be simplified to ΔF (Hz) = $-56.6 \times \Delta M_A$ (M_A indicates mass per unit area).

The electrostatic surface charges of the substrates were investigated by zeta potential measurement (ELSZ-1000, Otsuka Electronics, Japan).

Electrochemical Measurements: A three-electrode system was used, consisting of a CCF working electrode, an Ag/AgCl reference electrode, and a Pt counter electrode. To prepare the working electrode, the top end of the CCF was firmly connected to a copper wire using commercially available silver paste (ELCOAT P-100, CANS, South Korea). After the silver paste dried, it was further insulated with an epoxy adhesive. Cyclic voltammograms were obtained for the CCF electrode with a diameter of 200 µm, a length of 1.0 cm, and an external active surface area of 6.28 mm^2. The potential range was −0.6 to +0.6 V, and the measurements were performed using an electrochemical analyzer (Ivium-n-Stat, Ivium Technologies, Netherlands). All measurements were conducted in batch mode with 50 mL of PBS buffer (20 mmol L^{-1} phosphate and 140 mmol L^{-1} NaCl, pH 7.4) at 36.5 °C, without stirring, within an electrochemical cell. The inter-electrode distance between the anode and cathode electrode was ≈1 cm, and no membrane was used in this study.

To prevent electrical leakage during continuous operation power density measurements, one end of each hybrid BFC electrode was secured to a glass substrate using epoxy resin. The maximum anodic and cathodic current densities were determined by cyclic voltammetry (CV) at a constant voltage of +0.6 V for the anode and −0.6 V for the cathode, respectively. The normalized current density was calculated by subtracting the current density values measured in glucose-free PBS at +0.6 V for the anode and in oxygen-free PBS at −0.6 V for the cathode. Hybrid BFC power densities were determined by measuring the current output with a fixed external resistance (ranging from 1 kΩ to 10 MΩ) to control the cell potential. EIS measurements for the hybrid BFC electrodes were conducted over a frequency range of 0.2 Hz to 100 kHz with a perturbation amplitude of 0.01 V. The impedance spectra (Nyquist plots) obtained from the hybrid BFC electrochemical cell, represented by the real (Z') and imaginary (Z″) parts, were processed using Z View software (version 2.8d, Scribner Associates Inc., USA).

Laviron Model: The Laviron equation is a model used to determine the electron transfer coefficient (α) and the electron transfer reaction rate constant (k_s) of oxidizing and reducing species on the electrode surface, which are key parameters governing the electrode's electrochemical behavior. In general, the redox reaction of a material induced by a potential sweep may appear irreversible depending on the direction of the applied potential. This theory is expressed by the following equations:

$$\Delta E_{pc} = -\frac{RT}{\alpha nF}\ln\left(\frac{\alpha}{|m|}\right) = -\frac{RT}{\alpha nF}\ln\left(\nu\frac{\alpha nF}{RTk_s}\right) = -\frac{RT}{\alpha nF}\ln(\nu) - \frac{RT}{\alpha nF}\ln\left(\frac{\alpha nF}{RTk_s}\right) = a_c x + b_c \tag{2}$$

$$a_c = -\frac{2.303RT}{\alpha nF},\ b_c = -\frac{2.303RT}{\alpha nF}\log\left(\frac{\alpha nF}{RTk_s}\right),\ x = \log(\nu) \tag{3}$$

$$\Delta E_{pa} = \frac{RT}{(1-\alpha)nF}\ln\left(\frac{(1-\alpha)}{m}\right) = \frac{RT}{(1-\alpha)nF}\ln\left(\nu\frac{(1-\alpha)nF}{RTk_s}\right) = \frac{RT}{(1-\alpha)nF}\ln(\nu) + \frac{RT}{(1-\alpha)nF}\ln\left(\frac{(1-\alpha)nF}{RTk_s}\right) = a_a x + b_a \tag{4}$$

$$a_a = \frac{2.303RT}{(1-\alpha)nF},\ b_a = \frac{2.303RT}{(1-\alpha)nF}\log\left(\frac{(1-\alpha)nF}{RTk_s}\right),\ x = \log(\nu) \tag{5}$$

$$\Delta E = E_{pc} - E^\circ \text{ or } E_{pa} - E^\circ \tag{6}$$

$$\log k_s = \alpha\log(1-\alpha) + (1-\alpha)\log\alpha - \log\left(\frac{RT}{nF\nu}\right) - \frac{\alpha(1-\alpha)nF\Delta E}{2.303RT} \tag{7}$$

The variables in the equations [R (universal gas constant, R = 8.314 J mol^{-1} K^{-1}), T (absolute temperature), α (charge transfer coefficient), F (faraday constant, = 96485 C), E_{pa} (peak anodic potential), E_{pc} (peak cathodic potential), E° (apparent formal redox potential), k_s (heterogeneous electron transfer rate constant), n (number of electrons transferred, n = 1), a_a (anodic curve slope), b_a (anodic curve intercept), a_c (cathodic curve slope), b_c (cathodic curve intercept), ν (scan rate), and x (logarithm of scan rate)] were utilized in the generalization of the Laviron model for redox substances. The heterogeneous electron transfer rate constant (k_s) can be computed by analyzing the intersection of two linear fits corresponding to the anodic and cathodic curves.[58]

These results exhibit good linearity with a small relative error of 2% (as reported in the literature) when $n\Delta E > 200$ mV.[46] According to the above equation, the maximum value of the dimensionless phase occurs at the same position as the maximum current value. Furthermore, in cyclic voltammetry, the maximum or minimum current value corresponds to the E_{pa} and E_{pc} points, respectively. Consequently, changes in peak current with cyclic voltage sweep rate confirmed the absence of diffusion, indicating a truly immobilized electrode.

Supporting Information

Supporting Information is available from the Wiley Online Library or from the author.

Acknowledgements

This work was supported by the National Research Foundation of Korea (NRF) grant funded by the Korea government (NRF-2021R1A2C3004151 and 2022R1A2C1009690). The authors also acknowledge support from KIST Institutional Program (2V09840-23-P025) and the KU-KIST Graduate School of Converging Science and Technology Program. Additionally, it was supported by "Regional innovation Strategy (RIS)" through the National Research Fund of Korea (NRF) funded by the Ministry of Education (MOE) (2022RIS-005).

Conflict of Interest

The authors declare no conflict of interest.

Data Availability Statement

The data that support the findings of this study are available from the corresponding author upon reasonable request.

Keywords

biofuel cells, electron transfer-intensified mediator, enzyme immobilization

Received: March 19, 2024
Revised: May 9, 2024
Published online:

[1] S. Updike, G. Hicks, *Nature* **1967**, *214*, 986.
[2] X. Xiao, H.-Q. Xia, R. Wu, L. Bai, L. Yan, E. Magner, S. Cosnier, E. Lojiu, Z. Zhu, A. Liu, *Chem. Rev.* **2019**, *119*, 9509.
[3] C. H. Kwon, M. Kang, M. Kwon, D. Nam, Y. Song, E. Yong, M.-K. Oh, Y. Kim, B. Yeom, J. H. Moon, S. W. Lee, J. Cho, *Appl. Phys. Rev.* **2022**, *9*, 021413.
[4] I. Jeerapan, J. R. Sempionatto, Wang, J., *Adv. Funct. Mater.* **2020**, *30*, 1906243.
[5] A. Ruff, F. Conzuelo, W. Schuhmann, *Nat. Catal.* **2020**, *3*, 214.
[6] C. H. Kwon, S.-H. Lee, Y.-B. Choi, J. A. Lee, S. H. Kim, H.-H. Kim, G. M. Spinks, G. G. Wallace, M. D. Lima, M. E. Kozlov, R. H. Baughman, S. J. Kim, *Nat. Commun.* **2014**, *5*, 3928.
[7] N. Mano, F. Mao, A. Heller, *J. Am. Chem. Soc.* **2002**, *124*, 12962.
[8] X. Xiao, K. D. McGourty, E. Magner, *J. Am. Chem. Soc.* **2020**, *142*, 11602.
[9] D. Lee, S. H. Jeong, S. Yun, S. Kim, J. Sung, J. Seo, S. Son, J. T. Kim, L. Susanti, Y. Jeong, S. Park, K. Seo, S. J. Kim, T. D. Chung, *Biosens. Bioelectron.* **2021**, *171*, 112746.
[10] R. Ghosh, K. Y. Pin, V. S. Reddy, W. A. D. M. Jayathilaka, D. Ji, W. Serrano-Garcia, S. K. Bhargava, S. Ramakrishna, A. Chinnappan, *Appl. Phys. Rev.* **2020**, *7*, 041309.
[11] M. Rasmussen, R. E. Ritzmann, I. Lee, A. J. Pollack, D. Scherson, *J. Am. Chem. Soc.* **2012**, *134*, 1458.
[12] N. Mano, *Bioelectrochemistry* **2019**, *128*, 218.
[13] A. Ramanavicius, A. Kausaite, A. Ramanaviciene, *Sens. Actuators, B* **2005**, *111*, 532.
[14] X. Li, D. Li, Y. Zhang, P. Lv, Q. Feng, Q. Wei, *Nano Energy* **2020**, *68*, 104308.
[15] M. H. Kabir, E. Marquez, G. Djokoto, M. Parker, T. Weinstein, W. Ghann, J. Uddin, M. M. Ali, M. M. Alam, M. Thompson, A. S. Poyraz, H. Z. Msimanga, M. M. Rahman, J. Cramer, *ACS Appl. Mater. Interfaces* **2022**, *14*, 24229.
[16] N. Lalaoui, P. Rousselot-Pailley, V. Robert, Y. Mekmouche, R. Villalonga, M. Holzinger, S. Cosnier, T. Tron, A. L. Goff, *ACS Catal.* **2016**, *6*, 1894.
[17] J. W. Gallaway, B. S. A. Calabrese, *J. Am. Chem. Soc.* **2008**, *130*, 8527.
[18] K. Elouarzaki, D. Cheng, A. C. Fisher, J.-M. Lee, *Nat. Energy* **2018**, *3*, 574.
[19] A. Heller, *J. Phys. Chem. A* **1992**, *96*, 3579.
[20] Y. Degani, A. Heller, *J. Am. Chem. Soc.* **1989**, *111*, 2357.
[21] W. Schuhmann, T. J. Ohara, H.-L. Schmidt, A. Heller, *J. Am. Chem. Soc.* **1991**, *113*, 1394.
[22] P. N. Bartlett, V. Q. Bradford, R. G. Whitaker, *Talanta* **1991**, *38*, 57.
[23] C. Taylor, G. Kenausis, I. Katakis, A. Heller, *J. Electroanal. Chem.* **1995**, *396*, 511.
[24] S. M. Zakeeruddin, D. M. Fraser, M.-K. Nazeeruddin, M. Gratzel, *J. Electroanal. Chem.* **1992**, *337*, 253.
[25] B. A. Gregg, A. Heller, *Anal. Chem.* **1990**, *62*, 258.
[26] A. Heller, B. Feldman, *Chem. Rev.* **2008**, *108*, 2482.
[27] A. Heller, *Curr. Opin. Chem. Biol.* **2006**, *10*, 664.
[28] Z. Zhong, L. Qian, Y. Tan, G. Wang, L. Yang, C. Hou, A. Liu, *J. Electroanal. Chem.* **2018**, *823*, 723.
[29] N. Mano, F. Mao, A. Heller, *J. Am. Chem. Soc.* **2003**, *125*, 6588.
[30] S. Yoshino, T. Miyake, T. Yamada, K. Hata, M. Nishizawa, *Adv. Energy. Mater.* **2013**, *3*, 60.
[31] S. Yin, X. Liu, Y. Kobayashi, Y. Nishina, R. Nakagawa, R. Yanai, K. Kimura, T. Miyake, *Biosens. Bioelectron.* **2020**, *165*, 112287.
[32] I. Cho, Y. Song, S. Cheong, Y. Kim, J. Cho, *Small* **2020**, *16*, 1906768.
[33] K. K. Kanazawa, J. G. Gordon, *Anal. Chem.* **1985**, *57*, 1770.
[34] E. Yong, D. Nam, Y. Kim, K. Kim, B.-H. Kim, Y. Ko, J. Cho, *Energy Storage Mater.* **2023**, *60*, 102813.
[35] Y. Song, J. Cho, *Nanoscale* **2020**, *12*, 20141.
[36] J. Cho, K. Char, *Langmuir* **2004**, *20*, 4011.
[37] Y. Song, S. Lee, Y. Ko, J. Huh, Y. Kim, B. Yeom, J. H. Moon, J. Cho, *Adv. Funct. Mater.* **2022**, *32*, 2106438.
[38] D. Yoo, S. S. Shiratori, M. F. Rubner, *Macromolecules* **1998**, *13*, 4309.
[39] S. S. Shiratori, M. F. Rubner, *Macromolecules* **2000**, *33*, 4213.
[40] Y. Wang, M. Sarkar, A. E. Smith, A. S. Krois, G. J. Pielak, *J. Am. Chem. Soc.* **2012**, *134*, 16614.
[41] J. Ko, C. Kim, D. Kim, Y. Song, S. Lee, B. Yeom, J. Huh, S. Han, D. Kang, J.-S. Koh, J. Cho, *Sci. Robot.* **2022**, *7*, eabo6463.
[42] C. Yoo, S. Lee, Y. Song, W. Chang, M. K. Park, Y. Ko, J. Cho, *Carbon Energy* **2023**, *5*, e335.
[43] M. Gu, B.-S. Kim, *Acc. Chem. Res.* **2021**, *54*, 57.
[44] L. Lipani, B. G. R. Dupont, F. Doungmene, F. Marken, R. M. Tyrrell, R. H. Guy, A. Ilie, *Nat. Nanotechnol.* **2018**, *13*, 504.
[45] W. Luo, C. Zhu, S. Su, D. Li, Y. He, Q. Huang, C. Fan, *ACS Nano* **2010**, *4*, 7451.
[46] E. Laviron, *J. Electroanal. Chem.* **1979**, *101*, 19.
[47] W. Chen, S. Chen, *Angew. Chem., Int. Ed.* **2009**, *48*, 4386.
[48] A. Zebda, C. Gondran, A. L. Goff, M. Holzinger, P. Cinquin, S. Cosnier, *Nat. Commun.* **2011**, *2*, 370.
[49] Y. Yan, W. Zheng, L. Su, L. Mao, *Adv. Mater.* **2006**, *18*, 2639.
[50] S. C. Barton, M. Pickard, R. Vazquez-Duhalt, A. Heller, *Biosens. Bioelectron.* **2002**, *17*, 1071.
[51] A. J. Bandodkar, J. M. You, N. H. Kim, Y. Gu, R. Kumar, A. M. V. Mohan, J. Kurniawan, S. Imani, T. Nakagawa, B. Parish, M.

Parthasarathy, P. P. Mercier, S. Xu, J. Wang, *Energy Environ. Sci.* **2017**, *10*, 1581.
[52] M. Liu, R. Zhang, W. Chen, *Chem. Rev.* **2014**, *114*, 5117.
[53] J. Hernandez, J. Solla-Gullon, E. Herrero, A. Aldaz, J. M. Feliu, *J. Phys. Chem. C* **2007**, *111*, 14078.
[54] A. A. Babadi, W. A. A. Q. I. Wan-Mohtar, J.-S. Chang, Z. Ilham, A. A. Jamaludin, G. Zamiri, O. Akbarzadeh, W. J. Basirun, *Int. J. Hydrogen Energy* **2019**, *44*, 30367.
[55] W. Jia, X. Wang, S. Imani, A. J. Bandodkar, J. Ramirez, P. P. Mercier, J. Wang, *J. Mater. Chem. A* **2014**, *2*, 18184.
[56] M. Brust, M. Walker, D. Bethell, D. J. Schiffrin, R. Whyman, *J. Chem. Soc., Chem. Commun.* **1994**, *7*, 801.
[57] T. J. Ohara, R. Rajagopalan, A. Heller, *Anal. Chem.* **1993**, *65*, 3512.
[58] K. Takada, P. Gopalan, C. K. Ober, H. D. Abruna, *Chem. Mater.* **2001**, *13*, 2928.